Comparison of first moment STEM with conventional differential phase contrast and the dependence on electron dose

Comparison of first moment STEM with conventional differential phase contrast and the dependence on electron dose

Knut Müller-Caspary[a,b,*], Florian F. Krause[c], Florian Winkler[b], Armand Béché[a], Johan Verbeeck[a], Sandra VanAert[a], Andreas Rosenauer[c]

[a]*EMAT, University of Antwerp, Groenenborgerlaan 171, B-2020 Antwerpen, Belgium*
[b]*Ernst-Ruska Centre for Microscopy and Spectroscopy with Electrons, Forschungszentrum Jülich, Wilhelm-Johnen-Strasse, 52425 Jülich, Germany*
[c]*Institute for Solid State Physics, University of Bremen, Otto-Hahn-Allee 1, 28359 Bremen, Germany*

Abstract

This study addresses the comparison of scanning transmission electron microscopy (STEM) measurements of momentum transfers using the first moment approach and the established method that uses segmented annular detectors. Using an ultrafast pixelated detector to acquire four-dimensional, momentum-resolved STEM signals, both the first moment calculation and the calculation of the differential phase contrast (DPC) signals is done for the same experimental data. In particular, we investigate the ability to correct the segment-based signal to yield a suitable approximation of the first moment for cases beyond the weak phase object approximation. It is found that the measurement of momentum transfers using segmented detectors can approach the first moment measurement as close as $0.13\,h/nm$ in terms of a root mean square (rms) difference in $10\,nm$ thick $SrTiO_3$ for a detector with 16 segments. This amounts to 35% of the rms of the momentum transfers.

In addition, we present a statistical analysis of the precision of first moment STEM as a function of dose. For typical experimental settings with recent hardware such as a Medipix3 Merlin camera attached to a probe-corrected STEM, we find that the precision of the measurement of momentum transfers stagnates above certain doses. This means that other instabilities such as specimen drift or scan noise have to be taken into account seriously for measurements that target, e.g., the detection of bonding effects in the charge density.

Keywords: Scanning Transmission Electron Microscopy, Differential Phase Contrast, Momentum-resolved STEM, Pixelated STEM.

1. Introduction

Since the time when differential phase contrast (DPC) imaging [1–3] was introduced in the field of scanning transmission electron microscopy, it has found a wide range of applications. These include the high-contrast imaging of magnetic domains [4–6] as well as the investigation of electric fields [7], even down to the atomic scale [8, 9]. In recent years, methodological research on DPC strongly focused on conditions that allow for the quantitative interpretability of the signal, targeting the measurement of the angular deflection of the STEM probe caused by the specimen. Subsequently, the measurement of electric or magnetic fields at the absolute scale [10–12] became feasible. This recently lead to DPC measurements based on first moment detection in diffraction space as had been proposed earlier [3], but rendered impracticable even after the introduction of digital image registration due to

the very low frame rates of, e.g., charge-coupled devices (CCDs) [13].

With the introduction of ultrafast cameras to STEM [14–19], a drastic development took place. The wealth of details recorded in the diffraction patterns can now be evaluated so as to obtain information about the phase of the specimen exit wave using various techniques, namely DPC based on (virtual) segmented rings, first-moment STEM, or ptychography [20, 21]. In total, these techniques add to established ones such as off-axis electron holography [22–24] or focal series reconstruction [25] which are based on plane-wave illumination. It is obvious that, from the scientific point of view, the measurement of a certain specimen parameter must be independent of the method used, while applicability, data treatment, accuracy, precision and dose characteristics can still vary significantly for the different approaches. This suggests a comprehensive comparison of these aspects among the techniques mentioned above.

In this work, we first focus on the comparison of first-moment STEM with DPC based on virtual segmented detectors, referred to as FM-STEM and sDPC in the following. After a brief methodological summary, we use

---

[*]Corresponding author. Tel.: +49 2461 61 85237
Email address: `k.mueller-caspary@fz-juelich.de` (Knut Müller-Caspary)

experimental momentum-resolved STEM data of $SrTiO_3$ acquired with a Medipix3 [15] detector to investigate the quantitative agreement between the momentum transfers measured by both techniques. This comparison has the advantage that the identical experimental data can be used, so that any difference in the results can be attributed directly to the method.

In the second part, we address the dose dependence of precisions for signals evaluated from momentum-resolved STEM data, such as the momentum transfer, its divergence, as well as conventional signals, e.g., (annular) bright and annular dark field images. To this end, we recorded series of momentum-resolved STEM data using different doses and analyse the result using statistical methods.

The study takes place on the level of momentum transfer measurement and does not intend to provide details about, e.g., electric fields, potentials or charge densities. This strategy was chosen because the momentum transfer or, equivalently, the angular deflection, or phase, is the physical observable whereas derived quantities require approximate assumptions as to the interaction with the specimen. In other words, if the momentum transfer is already measured inaccurately or imprecisely, the same applies to the electric field measurement which, additionally, is constrained to very thin specimens.

2. Experiment

Aberration-corrected STEM measurements have been performed at the FEI Titan X-Ant-EM microscope at the EMAT institute in Antwerp, Belgium. The microscope was operated at $300\,kV$ with a STEM semi-convergence angle of $22.9\,mrad$. Momentum-resolved STEM data of $SrTiO_3$ was recorded by scanning the beam over the specimen and acquiring diffraction patterns for each scan position on a Medipix3 Merlin camera with a single 256×256 Si chip. The reciprocal space sampling was approximately $0.58\,mrad$ per Medipix pixel. The dose was varied by using different camera frame times between $10\,\mu s$ and $6\,ms$ on top of a gap time of $412\,\mu s$ imposed by the Medipix3 chip for 6 bit acquisition in single pixel mode. For dwell times of $6\,ms$, a depth of 12 bit was used, resulting in twice the gap time. For the Medipix detector operated in single pixel mode, only one of the two counting electronics per pixel is used, for which this so-called gap time puts a minimum to the duration of one Medipix recording in which no signal is acquired. Therefore, we refer to the actual duration of data collection as the frame time, keeping in mind that the total duration is always the sum of frame and gap time, which we synchronised with the dwell time of the STEM probe at each scan pixel. The detected dose is plotted in Fig. 1 (a). For each time setting, a momentum-resolved 128×128 STEM scan has been recorded with a STEM pixel size of $17.8\,pm$.

The specimen thickness shown in Fig. 1 (b) has been measured by recording both an overview STEM image and a detector scan of the Fischone 3000 detector which
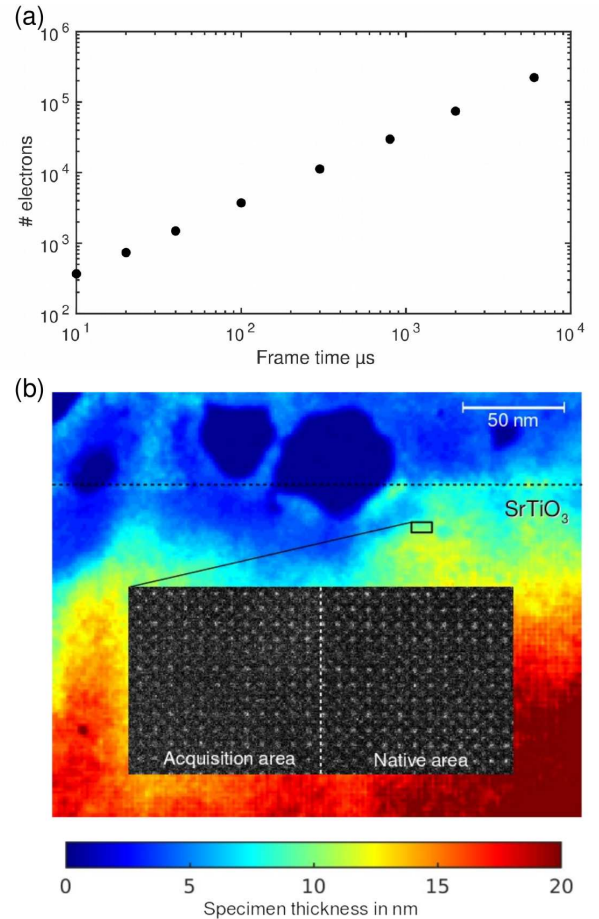

Figure 1: (a) Average number of electrons detected with the Medipix detector in each of the series for the full 128×128 scan versus the frame time. Note that the dwell time of the STEM probe was longer due to a gap time of the detector as mentioned in the text. (b) Thickness map in the vicinity of the region where the dose series was acquired (black rectangle), determined by calibrated STEM imaging compared with simulations. The inset shows a conventional STEM image taken afterwards showing the multiply exposed region next to a native area. The thickness in the investigated area is approximately $10\,nm$.

was operated in its linear range. As detailed in Ref. 26, the scattered intensity in the range $46 - 215$ mrad was normalised to that of the incoming beam, and compared with its thickness-dependent simulated counterpart. Because only very low thicknesses are relevant here, we used the multislice algorithm employing the absorptive potential approximation as implemented in the STEMsim software [27, 28].

3. Methodological summary

3.1. First moment STEM

Four-dimensional STEM, pixelated STEM, scanning diffraction and momentum-resolved STEM are terminologies that are currently used synonomously to describe the acquisition of diffraction patterns at each position of a scanning electron probe. Here, we refer to this technique as momentum-resolved STEM, being a distinct expression of the physical spaces explored. Among the vast amount of possibilites to evaluate momentum-resolved STEM data, first moment imaging is one approach to measure the angular deflection of the STEM probe.

By definition the first moment, also referred to as center of gravity or mass (COG or COM) of a recorded diffraction pattern, is identical to the average momentum of the electrons perpendicular to the optical axis[11]. It is defined as

$$\langle \vec{p}_\perp \rangle = \iint\limits_{-\infty}^{\infty} \vec{p}_\perp \cdot I(p_x, p_y) \, \mathrm{d}p_x \mathrm{d}p_y \quad , \tag{1}$$

where $I(p_x, p_y)$ represents the measured (normalised) intensity in momentum space and $\vec{p}_\perp = (p_x, p_y)$ the component of the momentum perpendicular to the optical axis. By defining $\langle \vec{p}_\perp \rangle = 0$ for the incident probe, $\langle \vec{p}_\perp \rangle$ is equal to the average momentum *transfer*. If $I(p_x, p_y)$ is replaced by the wave function times its complex conjugate, $\Psi(p_x, p_y)\Psi^*(p_x, p_y)$, the identity of Eq. (1) with the definition of the quantum mechanical expectation value for the momentum transfer in momentum space becomes obvious[11]. Recording the two-dimensional distribution of the intensity in diffraction space on a pixelated detector and calculating the first moment of $I(p_x, p_y)$ hence provides direct access to $\langle \vec{p}_\perp \rangle$. Of course, pixelation is a discretisation of Eq. (1), and the integration limits are finite due to the field of view of the camera. However, it has been shown earlier that the first moment converges rather quickly as a function of reciprocal space cutoffs beyond the Ronchigram diameter, and when using samplings better than a few mrad per camera pixel[11].

It is noteworthy that the identification of the first moment with the average momentum transferred to the STEM probe by interaction with the specimen holds in general, also in the presence of multiple scattering in thick specimens. However, great care must be taken when interpreting the momentum transfer directly in terms of projection-averaged electric fields. This has only been successful for extremely thin specimens based on the phase approximation so far. In fact, the momentum transfer is proportional to $\langle \Psi | \vec{E}_\perp | \Psi \rangle$ integrated over the specimen thickness as a result of Ehrenfest's theorem[10]. This essentially involves the integration over the electric field distribution in three dimensions, weighted by the local intensity of the electron wave inside the specimen which is subject to multiple scattering and propagation and is usually not known.

A related quantity is the divergence div$\langle \vec{p}_\perp \rangle$ of the vector field in Eq. (1). It reflects the sources and sinks of momentum transfer, and it has been identified to be very sensitive to light atoms, such as oxygen. For thin specimens where the phase approximation is valid, div$\langle \vec{p}_\perp \rangle$ is proportional to the charge density.

3.2. Segmented DPC detector approximation

Obviously, FM-STEM as described above imposes high challenges on aquisition hardware, data handling and data processing which became available for (S)TEM applications in this decade only. Therefore, the established DPC setup consists of segmented detectors which are usually circular and divided into segments in both radial and azimuthal direction. In this way, dwell times of the STEM probe in the microsecond range can be achieved in standard manner. This is still three orders of magnitude faster than FM-STEM based on contemporary pixelated detectors. An example with 16 segments is shown in Fig. 2(b). The detectors are positioned symmetrically around the optical axis, and the intensity on each of the segments is recorded individually. Afterwards, the intensity is multiplied with the geometrical center of the segment, all segments are summed up and the result is divided by the total intensity. In comparison with FM-STEM, this would be a formally equal implementation of Eq. (1) in polar coordinates for an infinite number of segments. However, established setups for DPC measurements with segmented detectors use a rather coarse discretisation of 4 to 16 segments[2, 29] for practical reasons. A more detailed description of the sDPC approach is given in Refs. [30–32].

It is worth mentioning that sDPC has found versatile applications, such as the imaging of magnetic domain walls[4, 5], the mapping of electric polarisation fields[7, 33], the high-contrast imaging of soft matter[34, 35], or the detection of electric fields at atomic resolution[8]. For the majority of these cases, the question to which extent the direct interpretation of sDPC signals approximates FM-STEM in terms of the accurate measurement of the momentum transfer might be of secondary importance for several reasons. First, sDPC is often used to provide high contrast in arbitrary units, e.g., in soft or magnetic matter, to investigate the structure and shape of, e.g., domain walls. Second, sDPC can be shown to be accurate for weak phase objects. Third, the quantitative interpretation of sDPC data obtained from strong phase objects and thick specimens is usually compared with accompanying simulations in cases where the specimen details are sufficiently well known.

However, at least two major applications exist that motivate the quantitative comparison of the sDPC and the FM-STEM technique provided in the following. First, the direct and quantitative interpretability between $\langle \vec{p}_\perp \rangle$ in Eq. (1) and the projection average of the local atomic-scale electric field is justified within the phase approximation, while the direct quantification of sDPC signals is usually based on weak phase objects. Second, the quantitative measurement of $\langle \vec{p}_\perp \rangle$ can have a justification on its own, even when the immediate conversion to, e.g., the electric field at a certain STEM scan pixel is not possible. For example, averaging $\langle \vec{p}_\perp \rangle$ over a unit cell can provide a quantitative measure of the beam deflection owing to meso-scale electric fields under certain conditions[11]. For many other cases, both sDPC and FM-STEM require accompanying simulations.

3.3. Correction of sDPC measurements

In the context of the quantification of the measurement of mmomentum transfers by sDPC, several correction schemes exist to extend the range of validity of this approach by taking the known detector geometry into account[36]. By construction, sDPC bins the electrons in each segment regardless of their exact impact position or it does not detect them at all due to the limited detector solid angle, which covers the diffraction pattern only partly. This suggests to check to which extent the following correction schemes can improve the accuracy of sDPC.

In phase object approximation (POA), the specimen is represented by a pure phase object $O(\mathbf{r}) = \exp\left[\mathrm{i}\phi(\mathbf{r}) \right]$ in real space with $\phi(\mathbf{r})$ the object phase. If the POA holds, the intensity distribution in the diffraction pattern will not be totally arbitrary. This can be exploited for correction schemes based on a transfer function $T_\alpha(\mathbf{k})$ that describes the transfer of the object function to the average momentum transfer,

$$\mathscr{F}\left\{ \langle \vec{p}_\perp \rangle(\mathbf{R}) \right\}_\alpha (\mathbf{k}) = \frac{h}{2\pi} T_\alpha(\mathbf{k}) \, \mathscr{F}\left\{ \nabla\phi(\mathbf{r}) \right\}_\alpha (\mathbf{k}) \quad . \quad (2)$$

Here, $\langle \vec{p}_\perp \rangle(\mathbf{R})$ is the average momentum transfer measured at probe position $\mathbf{R}$ and α denotes the lateral direction (e.g. x or y). The vectors $\mathbf{r}$ and $\mathbf{k}$ represent direct and reciprocal specimen coordinates and h is the Planck constant.

For FM-STEM, the transfer function within the POA is isotropic and therefore independent of α. It is given by the Fourier transform of the intensity $I_0(\mathbf{r})$ of the STEM probe,

$$T_\alpha^{\mathrm{FM}}(\mathbf{k}) = \mathscr{F}\left\{ I_0(\mathbf{r}) \right\}(\mathbf{k}) \quad , \quad (3)$$

as has been demonstrated in Ref. [11].

For sDPC, the $T_\alpha(\mathbf{k})$ is not isotropic, as the orientation of the segments determines preferred directions. For the present work, we use the transfer function that has been derived from the weak phase object approximation (WPOA) originally in detail in Refs. [31, 32]. In addition, approaches have been reported that go beyond the
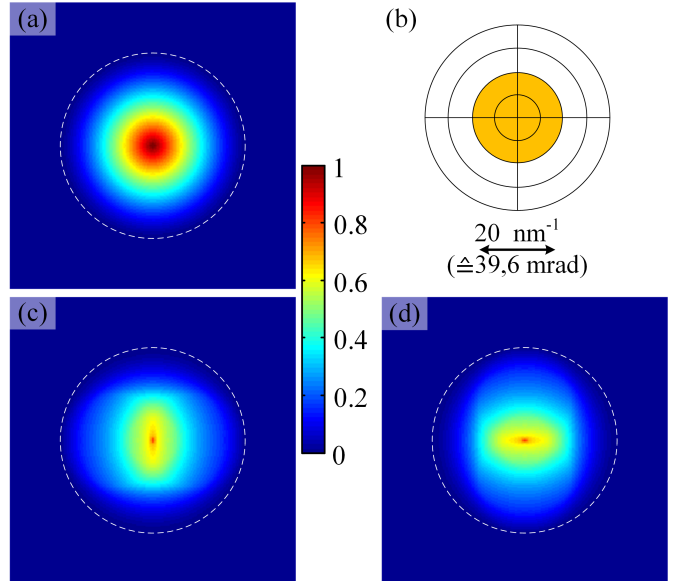

Figure 2: Comparison of the differential phase contrast transfer functions $T_\alpha(\mathbf{k})$ for FM-STEM (a) and sDPC in x (c) and y (d) direction for the detector geometry shown in (b): While $T_\alpha(\mathbf{k})$ is isotropic for FM-STEM, the contrast transfer in sDPC is anisotropic. The displayed scalebar and colorbar apply to all graphs. The orange area in (b) indicates the probe aperture of 22.9 mrad radius, i.e. the bright field disc, while the dashed circles in (a), (c) and (d) have twice this radius.

WPOA[30, 37], however, this is at the cost of the linearity of Eq. (2), which makes correction or deconvolution schemes more difficult. $T_\alpha(\mathbf{k})$ for sDPC then reads

$$\begin{aligned} T_\alpha^{\mathrm{sDPC}}(\mathbf{k}) &= \frac{1}{\mathbf{k}_\alpha} \int \mathrm{d}k' A(\mathbf{k}') D_\alpha(\mathbf{k}') \\ &\cdot \left(A(\mathbf{k}' - \mathbf{k}) \exp\left[-\mathrm{i}\chi(\mathbf{k}' - \mathbf{k}) + \mathrm{i}\chi(\mathbf{k}') \right] \right. \\ &\left. - A(\mathbf{k}' + \mathbf{k}) \exp\left[-\mathrm{i}\chi(\mathbf{k}' + \mathbf{k}) - \mathrm{i}\chi(\mathbf{k}') \right] \right) . \end{aligned} \quad (4)$$

$A(\mathbf{k})$ represents the probe aperture function, $\chi(\mathbf{k})$ denotes the probe aberration function. The function $D(\mathbf{k})$ describes the sensitivity of the sDPC detector such that each impact position $\mathbf{k}$ is assigned the detector output, which is usually the geometrical center of the respective segment. Figure 2 shows a comparison of the transfer functions for both methods. For the limit of an infinite number of radial and azimuthal segments Eq. (4) turns into Eq. (3).

Having calculated the transfer functions for both methods, different strategies for the correction are possible. Ref. [32] proposes a deconvolution by inverting Eq. (2) to calculate the gradient of the object phase, which is the electric field in POA. However, the electric field is a-priori unknown and the conversion is dependent on how well the POA holds. Two correction schemes for sDPC measurements of the momentum transfer will be used in the following. As proposed in Ref. [31], the function $D(\mathbf{k})$ is varied so as to make $T^{\mathrm{sDPC}}(\mathbf{k})$ as similar to $T^{\mathrm{FM}}(\mathbf{k})$ as possible. In this way, the transfer function for sDPC is »a-priori adapted« to come as close to the ideal detector as possible.

4

Primarily, we used the following approach, which we refer to as »corrected« sDPC. In this case, the Fourier transform of the uncorrected sDPC signal is multiplied with the quotient of the transfer functions of FM-STEM and sDPC,

$$\mathscr{F}\left\{\langle\vec{p}_\perp\rangle_{\mathrm{corr.}}^{\mathrm{sDPC}}(\mathbf{R})\right\}_\alpha(\mathbf{k}) = $$
$$\frac{T_\alpha^{\mathrm{FM}}(\mathbf{k})}{T_\alpha^{\mathrm{sDPC}}(\mathbf{k})}\,\mathscr{F}\left\{\langle\vec{p}_\perp\rangle_{\mathrm{uncorr.}}^{\mathrm{sDPC}}(\mathbf{R})\right\}_\alpha(\mathbf{k})\quad. \tag{5}$$

Because both transfer functions show a similar decay towards high frequencies and are bandwidth limited at twice the probe aperture radius, the quotient in Eq. (5) approaches 1 for large $\mathbf{k}$ and, at least for small aberrations, does neither diverge nor vanish. This makes the calculation in Eq. (5) relatively straight forward compared to other deconvolution schemes. In contrast to the a-priori adaption of the sensitivity this a-posteriori correction has the advantage that it can correct for the anisotropy of sDPC, which is not possible a-priori for a given detector geometry. On the other hand, the necessary Fourier transform can be problematic if the data shows significant amounts of scan noise.

4. Quantitative comparison of FM-STEM and sDPC results

To explore the accuracy of momentum transfer measurement of sDPC beyond the weak phase object approximation, the momentum-resolved dataset described in Sec. 2 (10 nm thick $SrTiO_3$) for the dwell time of $2000\,\mathrm{\mu s}$ was evaluated with both FM-STEM and sDPC. For FM-STEM this was done by a first moment calculation according to Eq. (1), for sDPC a virtual segmented detector sensitivity was generated and applied to the diffraction patterns. To ensure the best comparability, the diffraction patterns were cropped at the outer radius of the sDPC detector. Both values are hence based on exactly the same data.

Furthermore, the correction described in Section 3.3 was applied to the sDPC results. The calculations were done for three different detector geometries: First, a 4-segment detector with twice the radius of the probe aperture was used. Second, a 16-segment detector with 4 rings, each divided into 4 segments, with an outer radius of twice the aperture, was employed. Third, a slightly smaller 16-segment detector, where the probe radius was two thirds of the detector radius, was investigated.

A magnified cutout of the resulting momentum transfer vector fields is shown in Fig. 3, in which the used detector geometries are also displayed. For the FM-STEM data shown in black, a slight deviation from the expected radially symmetric fields at atomic sites is observed due to scan noise and specimen drift. However, as all displayed data has been derived from exactly the same diffraction patterns, this does not influence the comparison of the different approaches. The precision of measured parameters as a function of acquisition times is studied in detail in Sec. 5.

In qualitative respect, the sDPC results can approach the FM-STEM data partly for the 16-segment detectors in Fig. 3 (b,c), whereas the 4-segment data in Fig. 3 (a) show significant deviations from the first moment result. Contrasting the differences between sDPC and FM-STEM in Fig. 3 (b,c) with the different complexities of the experimental setups, i.e. the recording of 16 channels versus the recording of $256 \times 256 = 65536$ camera pixels at each scan position, the qualitative similarity of the vector fields is interesting. In that respect, one must also keep in mind that the data set corresponds to a specimen thickness of approximately 10 nm in $SrTiO_3$, which is far beyond the ranges of validity of the WPOA and the POA. However, typical STEM measurements are performed at much thicker specimens. Fig. 3 also shows the limitation of the correction schemes applied here, as they do not significantly improve the agreement with the FM-STEM result visually, or even decrease accuracy for some scan pixels. This also holds for the *a priori* adaption method applied in Fig. 3 (d). At least concerning the correction schemes of Section 3.3, we can conclude here that enhanced accuracy is rather achievable by a more dense sampling of the diffraction pattern than by correcting low-sampled experimental data. This can be attributed to the fact that the WPOA and in part even the POA are not justified at the present specimen thickness.

Focusing on the main goal of this section, the quantitative comparison of FM-STEM and sDPC, the directions of the momentum transfers measured by sDPC in Fig. 3 can still deviate from the first moments by $20-30°$ locally, especially in the vicinity of the Sr atom. In terms of the root mean square (rms) difference of the magnitudes of the momentum transfers measured by sDPC and FM-STEM, we find values of $0.347\,h\mathrm{nm}^{-1}$ and $0.31\,h\mathrm{nm}^{-1}$ for the uncorrected and the corrected sDPC data in Fig. 3 (a), respectively. Normalised to the rms of the momentum transfers themselves ($0.380\,h\mathrm{nm}^{-1}$), this means relative errors of 91 and 83%, respectively. The highest accuracy is found for the a-posteriori corrected large 16-segment detector, for which an rms deviation of $0.131\,h\mathrm{nm}^{-1}$ was calculated, corresponding to a relative deviation of 35%. The sDPC data for the other 16-segment detectors exhibit rms differences of less than $0.144\,h\mathrm{nm}^{-1}$ with respect to the first moments, corresponding to relative differences between 35 and 38%.

Other calculations with slightly changed detector radii confirmed that the differences to FM-STEM are not due to an inappropriately chosen detector size. Only for very large or small detectors the accuracy gets worse, but for the given specimen thickness the exact size does not have a large influence. Despite the strength of sDPC to approach the actual first moment measurement rather quickly with a very limited number of segments, significant differences to FM-STEM can be observed in a quantitative assessment, which should be kept in mind when using sDPC for, e.g., built-in electric fields. This is typically performed at elevated specimen thicknesses of several tens

of nanometers. For example, polarisation fields in piezo- or ferroelectrics cause momentum transfers in the order of $0.1\,h\mathrm{nm}^{-1}$. They are thus rather small and comparable to the deviations of sDPC found in Fig. 3, assuming a specimen thickness of a few tens of nanometers.

To shed light on the range of validity of the WPOA as a function of specimen thickness, a simulation study was conducted for SrTiO$_3$ in [001] orientation using the experimental conditions mentioned in Sec. 2. The same evaluation as described before was performed, and the relative rms deviation to the first moment result is displayed in Fig. 4 for the detector geometry in Fig. 2. Obviously, both the a-priori adaption and the a-posteriori correction do bring the sDPC close to the FM-STEM result at small thicknesses $< 1\,\mathrm{nm}$. For increasing thickness, the benefits of both correction schemes methods relativise rather quickly. Above $2\,\mathrm{nm}$, the raw sDPC signal is actually preferable. The small improvements observed in the experimental data are hence most likely not significant.

5. Dose dependent measurements

5.1. General considerations

Designing experiments so as to optimise accuracy and precision for the measurement of a parameter of interest, such as $\langle \vec{p}_\perp \rangle$ or div $\langle \vec{p}_\perp \rangle$, is a major challenge in quantitative electron microscopy. For example, the above studies addressed the difference in accuracy for fully momentum-resolved STEM and segmented detector-based DPC with respect to the measurement of the angular deflection of the electron probe. However, even for accurate measurements, precision is limited due to the unavoidable presence of noise[38]. Ideally, this limit should be imposed by Poisson counting statistics, i.e. the dose one uses in experiment. At first sight, this implies that a measurement becomes more precise the more dose is used. For example, doses between $5 \cdot 10^3 - 5 \cdot 10^6$ electrons per diffraction pattern have been simulated previously [11] to find that already $1.8 \cdot 10^4$ electrons would be sufficient to assure a root mean square error in the range of $0.05\,h/\mathrm{nm}$. At least in principle this would be sufficient to detect, e.g., bonding effects which alter momentum transfers by up to $0.2\,h/\mathrm{nm}$ in GaN, if counting statistics was the only limit to precision.

In this section, we address the basic dependence of precision on dose in practice for the measurement of $\langle \vec{p}_\perp \rangle$, div $\langle \vec{p}_\perp \rangle$ as well as bright field (BF), annular bright field (ABF) and annular dark field (ADF) STEM calculated from momentum-resolved STEM experiments. To this end, we scanned over the same region of approximately 5×5 SrTiO$_3$ unit cells with different frame times as shown in Fig. 1 (a). By acquiring a conventional high-resolution STEM image after this experiment, we assured that the investigated area did not degrade structurally in comparison to a native region, as depicted by the inset images in Fig. 1 (b).

Figure 5 shows a compilation of the different virtual images versus the frame times. Because the absolute values of the BF, ADF and ABF images scale with the number of electrons, the contrast has been adjusted to the range $0 \ldots 1$ for visual clarity. Note that the first moment and its divergence in the three columns on the right are shown at absolute contrast scale with limits indicated at the bottom. As a global trend for all six signals, a decrease of Poisson noise with increasing dwell time is observed as expected. However, for frame times above $300\,\mu\mathrm{s}$, significant structural distortions start to occur which is seen most obviously from the shear of the cubic unit cells. On a qualitative basis, this demonstrates that precision is furthermore governed by additional parameters such as specimen drift, scan noise, or more general, stability of the experimental setup. Although the frame time is increased by a factor of 20, the interpretability of the data acquired longer than $300\,\mu\mathrm{s}$ either stagnates or even decreases.

On a more quantitative concern, Fig. 6 shows the Fourier transform of div $\langle \vec{p}_\perp \rangle$ (left, modulus) and the azimuthal averages (right). Interestingly, no improvement is noticed after the lowest three frame times $10, 20$ and $40\,\mu\mathrm{s}$, while the drastic attenuation of contrast for all spatial frequencies is becoming obvious above $800\,\mu\mathrm{s}$ exposure. The obvious conclusion is that better counting statistics should rather be provided by increasing the probe current, and keeping the frame time at a minimum. On the other hand, existing ultrafast STEM cameras impose maximum frame rates in the kHz range which is still low compared to conventional STEM speeds. Moreover, the dynamic range of the STEM camera might be limited, and one also has to keep in mind that increasing the dose rate can lead to enhanced specimen damage.

In the following, we thus assume that, due to hardware constraints or the risk of specimen damage, the acquisition time is increased in order to enhance the precision. We use the data of Fig. 5 to investigate to which extent this strategy is reasonable.

5.2. Statistical analysis

Checking the precision of the measurement of a certain parameter such as the spatial distribution of $\langle \vec{p}_\perp \rangle$ or div$\langle \vec{p}_\perp \rangle$ in one unit cell of a crystal essentially requires the repetition of the experiment, i.e., the momentum-resolved STEM scan over the same unit cell, and the subsequent statistical analysis. In this study, this is approximated by analysing a set of 20 adjacent unit cells from one acquisition. It is hence assumed that each of these unit cells exhibits the same spatial distribution of, e.g., $\langle \vec{p}_\perp \rangle$. Due to the small size of $2 \times 2\,\mathrm{nm}$ this assumption should be sufficiently justified. Let $Q_i^\tau(u,v)_i$ be the spatial distribution of a measured parameter Q within one unit cell described by index i with internal coordinates $u, v \in [0 \ldots 1]$ and acquired with frame time τ, then

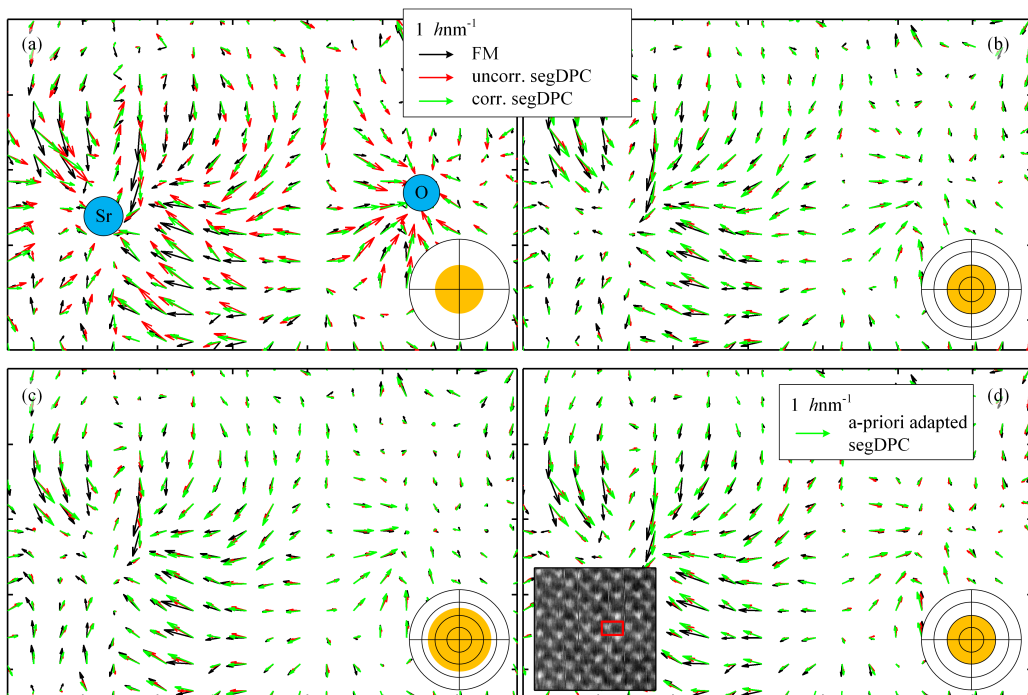$$\bar{Q}^\tau(u,v) = \frac{1}{N} \sum_i^N Q_i^\tau(u,v)$$

Figure 3: Average momentum transfer results for the measurement with 2000 µs dwell time from the area marked in in the lower left inset of (d) for different sDPC detectors: The black arrows represent the FM-STEM result, while red and green respectively show the uncorrected and corrected sDPC result. The detector geometries and sizes in relation to the probe aperture (orange circle) of 22.9 mrad are shown as insets. For (a) and (b) the outermost radius was twice this radius, for (c) it was 1.5 times as large. (d) is for the same detector as (b), but the green arrows represent the result of an a-priori adapted detector as described in the text.
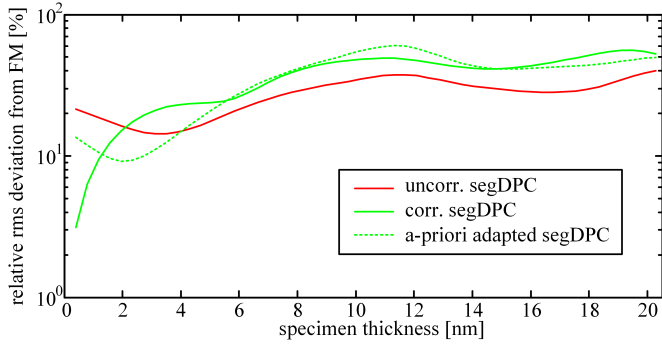
Figure 4: Results from a simulation study of [001]-SrTiO$_3$ for various thicknesses: The graph shows the relative rms deviation of sDPC from FM-STEM. Benefits of the correction schemes are only observed below 4 nm specimen thickness.
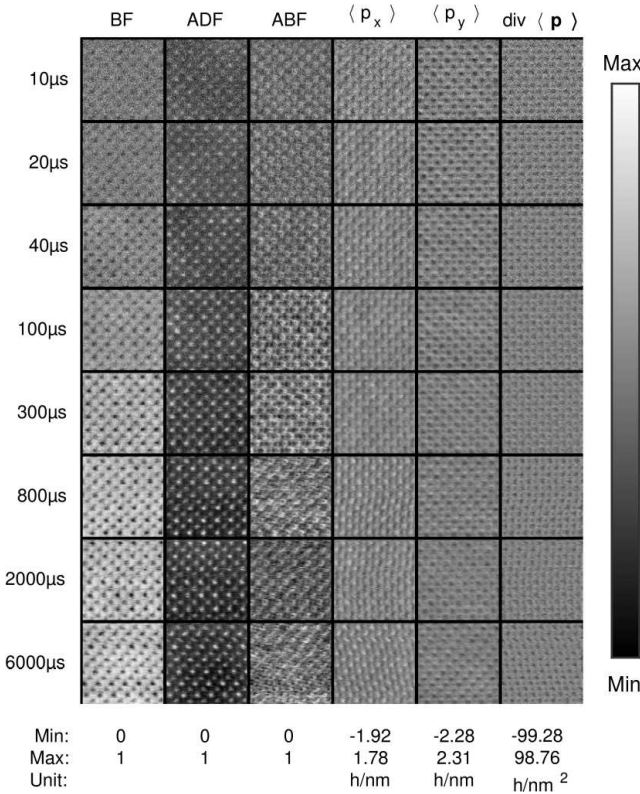

Figure 5: Signals generated from the momentum-resolved STEM data recorded with the Medipix camera using different frame times and corresponding STEM scan speeds, respectively. The bright field (BF) signal is the intensity sum over the Ronchigram, the annular dark field (ADF) image was calculated for an angular range of $31 - 54$ mrad, and the annular bright field (ABF) for $11.5 - 22.9$ mrad. $\langle p_{x,y} \rangle$ are the components of the momentum transfer perpendicular to the optical axis in units of Planck's constant $h = 6.62607$ Js as calculated from the first moment of the diffraction patterns.
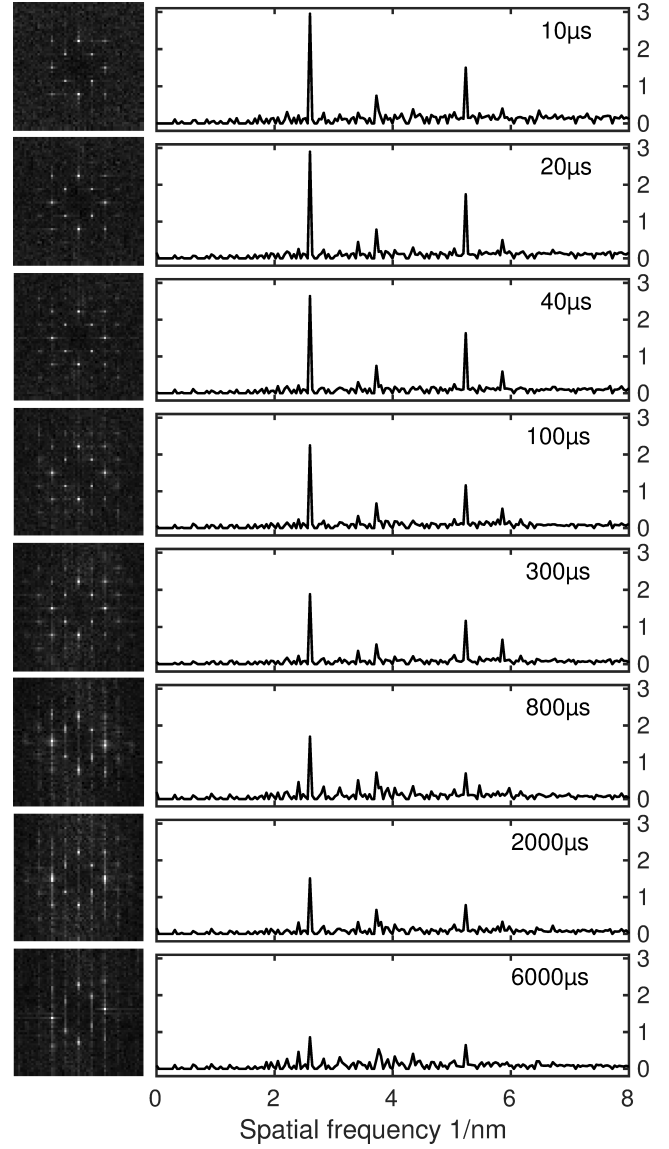

Figure 6: Fourier transforms of div $\langle \vec{p}_\perp \rangle$ in dependence of the frame time. On the right, the azimuthal averages are shown. The y-axis has arbitrary units, but exhibits the same scaling for all frame times.
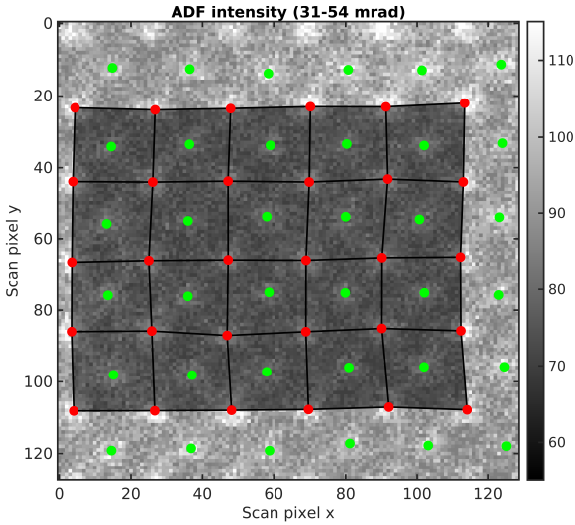
8

Figure 7: Detection of the atomic grid in an ADF image generated from the momentum-resolved STEM data set. Due to specimen drift primarily, the unit cells are distorted which is numerically corrected for by calculating affine or polynomial transforms using the ImageEval software [39].

is the mean spatial distribution of parameter Q within a unit cell determined from N independent measurements. By definition,

$$\sigma^\tau(u,v) = \sqrt{\frac{\sum_{i}^{N}\left(Q_i^\tau(u,v) - \bar{Q}^\tau(u,v)\right)^2}{N-1}} \qquad (6)$$

is the standard deviation of Q at each scan pixel u,v in the unit cell. The statistical analysis relies on the comparison of Q at exactly the same internal coordinates (u,v) which is most dominantly hindered by the specimen drift at elevated frame times.

To cope with this problem, we implemented a distortion correction for each unit cell in the ImageEval software [39], as illustrated exemplarily in Fig. 7. First, we detect the unit cell vertices of the cubic SrTiO$_3$ lattice in an ADF image and refine the positions to subpixel accuracy, for which parabolic, Gaussian fitting or centre of mass approaches are available. Then, these cells can be mapped onto the known cubic ones either by determining the corresponding affine or polynomial transforms as implemented in Matlab, or by explicitly expressing all pixel coordinates with respect to the basis vectors of the unit cell that contains these pixels, and then interpolating the signals $Q_{1...N}^\tau$ to a common grid of internal coordinates. In the present case, these three approaches yielded identical results.

Instead of showing the two-dimensional distribution $\sigma^\tau(u,v)$ for each frame time, we present this trend in a more compact manner. To this end, $\sigma^\tau(u,v)$ was averaged
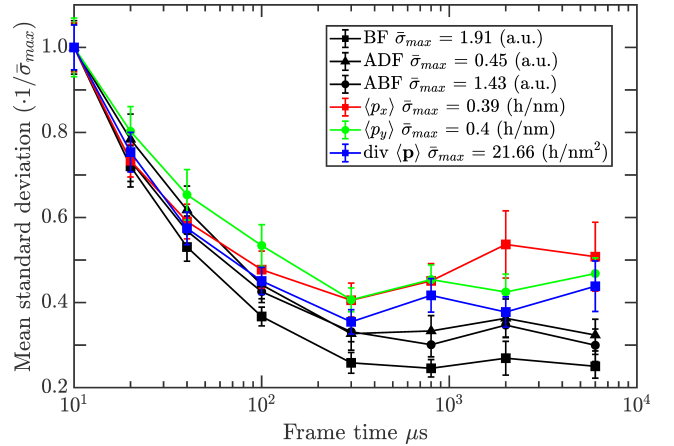

Figure 8: Frame time dependent standard deviations averaged over one unit cell for the BF, ADF, ABF signals as well as for the momentum transfer $\langle \vec{p}_\perp \rangle$ and its divergence. Increasing the frame time over $300-800\,\mu$s does not improve the precision of measured parameters anymore. The unit and the scale of the y-axis are given in teh legend.

in regions where the signal $\bar{Q}^\tau(u,v)$ was of comparable magnitude, for which we selected a patch of 3×3 pixels on each of the heavy atomic columns. The result, the mean standard deviation at these postions $\bar{\sigma}(\tau)$, is shown in Fig. 8. The trend is almost the same for all six signals. The standard deviation is maximum for the lowest frame time of $10\,\mu$s and then decreases up to frame times of $300-800\,\mu$s which would be the expected enhancement of precision due to improved counting statistics. However, the curves asymptotically approach a constant value between 0.2 and $0.5 \cdot \bar{\sigma}_{max}$, with a tendency to form a minimum such as the blue and red graphs, which, however, is not very significant in view of the confidence intervals given. Note that for thin specimens, these quantities would be directly proportional to the precisions for the measurement of the local electric field or the charge density whereas the BF, ADF or ABF signals do not directly represent specimen parameters.

The reasons for the lower limit to the precision in the present study can be manyfold, e.g., scan noise arising from inaccurate positioning of the STEM probe, vibrations of the specimen holder and instabilities of any probe-forming electron-optical element such as the lenses, the probe corrector, the monochromator, the high tension, the extraction voltage, the influence of the cooling system etc. Of course, the procedure to compensate for specimen drift as mentioned in conjunction with Fig. 7 might also exhibit a limited precision. Identifying which of those parameters plays the dominant role for the asymptotic behaviour towards nonzero standard deviation in Fig. 8 would be the key for improving precision further, of course. Let us assume that bonding effects in SrTiO$_3$ cause momentum transfer changes of the order of $0.2\,h/$nm, then the curves in Fig. 8 would exhibit practical relevance immediately, because the best precision for the local measurement of

$\langle \vec{p}_\perp \rangle$ would be approximately $0.16\,h/\mathrm{nm}$ which precludes conclusions on charge density fluctuations of the order of Bader charges as a measure of ionicity[40, 41].

6. Discussion and summary

The fact that the segments used in sDPC average over extended parts of the diffraction pattern had been one of the driving forces for the development of momentum-resolved STEM, especially FM-STEM as one discipline therein. In particular, sDPC is not able to capture the fine details of the intensity distribution in diffraction space. However, the motivation for the present study was to check to which extent this is really necessary, especially with the ability to correct for the detector geometry [31, 32], and the fact that sDPC measurements approach a first moment detection rather quickly when increasing the number of segments. However, our results show that measurements of the momentum transfer with the sDPC technique employing 4-16 segments should be taken with care when interpreted quantitatively, at least for the case study considered here, i.e. $SrTiO_3$ with a thickness of $10\,\mathrm{nm}$. Although this is beyond the thickness range where the weak phase or even the phase approximations hold and a direct conversion of the results to electric fields and charge densities would be possible, a different outcome of FM-STEM and sDPC can be observed.

One can argue that it is anyway necessary to conduct accompanying simulations in such cases to allow for accurate conclusions as to the atomic structure in both setups. To a certain extent, this is indeed true and supporting differential phase contrast measurements with simulations is common practice in literature[8, 10, 11, 42, 43]. In this context, two aspects should be kept in mind. First, the ranges of validity for the direct, quantitative interpretability of segment and first moment based differential phase contrast results are different owing to the implications of the weak phase approximation and the phase approximation. For example, single atom thick specimens, such as 2D materials, are not necessarily weak phase objects, but can be well described within the phase object approximation[44]. Second, the direct, quantitative measurement of the momentum transfer in thick specimens with strong dynamic scattering effects can be attractive for the mapping of external, mesoscale electric fields. For example, the momentum transfer averaged over a Bravais unit cell vanishes in centrosymmetric systems. In these cases, the residual of a unit cell average can be interpreted as caused by the external electric field [11], and it can hence be used to quantify this field at the scale of unit cells, which we regard as a future task. Moreover, the quantitative knowledge of the angular beam deflection in thick specimens might also be valuable to gain topological information, because inclined surfaces cause a momentum transfer, too.

In general, sDPC experiences high popularity mainly due to practical aspects. In particular, the speed of seg-

mented detectors is up to two orders of magnitude higher than that of available ultrafast cameras, and the FM-STEM requires partly advanced analyses of large four-dimensional data sets. However, recent improvements of the efficiency of data processing, e.g., in the LiberTEM project[45], or the introduction of ultrafast, non-pixelated, direct first moment detectors[46] are encouraging developments that have the potential to enhance the practical applicability of first moment STEM to that of sDPC and conventional STEM imaging. Consequently, first moment STEM currently takes the step to become a valuable technique for quantitative differential phase contrast imaging beyond the weak phase approximation and hence complements the range of applications of DPC STEM.

In an experimental study conducted under typical conditions, we additionally studied to which extent Poisson counting statistics limits the precision of FM-STEM. In the present case, we found that we are not Poisson-limited above frame times of $300 - 800\,\mu s$ anymore, where a stagnation or even decrease of precisions for BF, ADF, ABF and momentum transfer measurements are observed. For the momentum, the best precision was found to be approximately $0.16\,h/\mathrm{nm}$, which should only be improvable by increasing the stability of the experimental conditions during the acquisition time. This could involve reducing specimen drift or scan noise. However, it can be expected that the dependence of precision on dose will be similar in most situations, however, with a different scaling of the axes.

7. Acknowledgements

References

[1] H. Rose, Nonstandard imaging methods in electron microscopy, Ultramicroscopy 2 (1977) 251–267.
[2] N. H. Dekkers, H. de Lang, Differential Phase Contrast in a STEM, Optik 41 (1974) 452–456.
[3] E. M. Waddell, J. N. Chapman, Linear imaging of strong phase objects using asymmetrical detectors in STEM, Optik 54 (1979) 83–96.

[4] J. Chapman, P. Batson, E. Waddell, R. Ferrier, The direct determination of magnetic domain wall profiles by differential phase contrast electron microscopy, Ultramicroscopy 3 (1978) 203–214.

[5] R. Ploessl, J. N. Chapman, A. M. Thompson, J. Zweck, H. Hoffmann, Investigation of the micromagnetic structure of cross-tie walls in permalloy, J. Appl. Phys. 73 (1993) 2447–2452.

[6] C. W. Sandweg, N. Wiese, D. McGrouther, S. J. Hermsdoerfer, H. Schultheiss, B. Leven, S. McVitie, B. Hillebrands, J. N. Chapman, Direct observation of domain wall structures in curved permalloy wires containing an antinotch, J. Appl. Phys. 103 (2008) 093906.

[7] M. Lohr, R. Schregle, M. Jetter, C. Wächter, T. Wunderer, F. Scholz, J. Zweck, Differential phase contrast 2.0—Opening new "fields" for an established technique, Ultramicroscopy 117 (2012) 7–14.

[8] N. Shibata, S. D. Findlay, Y. Kohno, H. Sawada, Y. Kondo, Y. Ikuhara, Differential phase-contrast microscopy at atomic resolution, Nat. Phys. 8 (2012) 611–615.

[9] N. Shibata, T. Seki, G. Sánchez-Santolino, S. D. Findlay, Y. Kohno, T. Matsumoto, R. Ishikawa, Y. Ikuhara, Electric field imaging of single atoms, Nature Communications 8 (2017) 15631.

[10] K. Müller, F. F. Krause, A. Beche, M. Schowalter, V. Galioit, S. Löffler, J. Verbeeck, J. Zweck, P. Schattschneider, A. Rosenauer, Atomic electric fields revealed by a quantum mechanical approach to electron picodiffraction, Nature Comm. 5 (2014) 5653:1–8.

[11] K. Müller-Caspary, F. F. Krause, T. Grieb, S. Löffler, M. Schowalter, A. Béché, V. Galioit, D. Marquardt, J. Zweck, P. Schattschneider, J. Verbeeck, A. Rosenauer, Measurement of atomic electric fields and charge densities from average momentum transfers using scanning transmission electron microscopy, Ultramicroscopy 178 (2017) 62–80.

[12] A. Lubk, J. Zweck, Differential phase contrast: An integral perspective, Phys. Rev. A 91 (2015) 023805.

[13] J. C. H. Spence, J. M. Zuo, Large dynamic range, parallel detection system for electron diffraction and imaging 59 (1988) 2102–2105.

[14] K. Müller, H. Ryll, I. Ordavo, S. Ihle, L. Strüder, K. Volz, J. Zweck, H. Soltau, A. Rosenauer, Scanning transmission electron microscopy strain measurement from millisecond frames of a direct electron charge coupled device, Appl. Phys. Lett. 101 (2012) 212110.

[15] R. Plackett, I. Horswell, E. N. Gimenez, J. Marchal, D. Omar, N. Tartoni, Merlin: a fast versatile readout system for Medipix3, Journal of Instrumentation 8 (2013) C01038.

[16] V. B. Ozdol, C. Gammer, X. G. Jin, P. Ercius, C. Ophus, J. Ciston, A. M. Minor, Strain mapping at nanometer resolution using advanced nano-beam electron diffraction, Appl. Phys. Lett. 106 (2015) 253107.

[17] K. Müller-Caspary, A. Oelsner, P. Potapov, Two-dimensional strain mapping in semiconductors by nano-beam electron diffraction employing a delay-line detector, Appl. Phys. Lett. 107 (2015) 072110.

[18] M. W. Tate, P. Purohit, D. Chamberlain, K. X. Nguyen, R. Hovden, C. S. Chang, P. Deb, E. Turgut, J. T. Heron, D. G. Schlom, D. C. Ralph, G. D. Fuchs, K. S. Shanks, H. T. Philipp, D. A. Muller, S. M. Gruner, High dynamic range pixel array detector for scanning transmission electron microscopy, Microsc. Microanal. 22 (2016) 237–249.

[19] H. Ryll, M. Simson, R. Hartmann, P. Holl, M. Huth, S. Ihle, Y. Kondo, P. Kotula, A. Liebel, K. Müller-Caspary, A. Rosenauer, R. Sagawa, J. Schmidt, H. Soltau, L. Strüder, A pnccd-based, fast direct single electron imaging camera for tem and stem, J. Instrum. 11 (2016) P04006.

[20] T. J. Pennycook, A. R. Lupini, H. Yang, M. F. Murfitt, L. Jones, P. D. Nellist, Efficient phase contrast imaging in {STEM} using a pixelated detector. part 1: Experimental demonstration at atomic resolution, Ultramicroscopy 151 (2015) 160–167. Special Issue: 80th Birthday of Harald Rose; {PICO} 2015 – Third Conference on Frontiers of Aberration Corrected Electron Microscopy.

[21] H. Yang, R. N. Rutte, L. Jones, M. Simson, R. Sagawa, H. Ryll, M. Huth, T. J. Pennycook, M. L. H. Green, H. Soltau, Y. Kondo, B. G. Davis, P. D. Nellist, Simultaneous atomic-resolution electron ptychography and z-contrast imaging of light and heavy elements in complex nanostructures, Nature Comm. 7 (2016) 12532.

[22] F. Winkler, J. Barthel, A. H. Tavabi, S. Borghardt, B. E. Kardynal, R. E. Dunin-Borkowski, Absolute Scale Quantitative Off-Axis Electron Holography at Atomic Resolution, Phys. Rev. Lett. 120 (2018) 156101.

[23] G. Möllenstedt, H. Düker, Fresnelscher Interferenzversuch mit einem Biprisma für Elektronenwellen, Naturwissenschaften 42 (1955) 41.

[24] C. T. Koch, V. B. Özdöl, P. A. van Aken, An efficient, simple, and precise way to map strain with nanometer resolution in semiconductor devices, Appl. Phys. Lett. 96 (2010) 091901.

[25] W. M. J. Coene, A. Thust, M. Op de Beeck, D. van Dyck, Maximum-likelihood method for focus-variation image reconstruction in high resolution transmission electron microscopy, Ultramicroscopy 64 (1996) 109–135.

[26] A. Rosenauer, T. Mehrtens, K. Müller, K. Gries, M. Schowalter, P. V. Satyam, S. Bley, C. Tessarek, D. Hommel, K. Sebald, M. Seyfried, J. Gutowski, A. Avramescu, K. Engl, S. Lutgen, Composition mapping in InGaN by scanning transmission electron microscopy, Ultramicroscopy 111 (2011) 1316–1327.

[27] A. Rosenauer, M. Schowalter, STEMSIM-a new software tool for simulation of STEM HAADF Z-contrast imaging, in: A. G. Cullis, P. A. Midgley (Eds.), Springer Proceedings in Physics, volume 120, Springer, 2007, pp. 169–172. doi:10.1007/978-1-4020-8615-1_36.

[28] A. Rosenauer, M. Schowalter, J. T. Titantah, D. Lamoen, An emission-potential multislice approximation to simulate thermal diffuse scattering in high-resolution transmission electron microscopy, Ultramicroscopy 108 (2008) 1504–1513.

[29] N. Shibata, Y. Kohno, S. D. Findlay, H. Sawada, Y. Kondo, Y. Ikuhara, New area detector for atomic-resolution scanning transmission electron microscopy, J. Electron Microsc. 59 (2010) 473–479.

[30] I. Lazic, E. G. Bosch, S. Lazar, Phase contrast stem for thin samples: Integrated differential phase contrast, Ultramicroscopy 160 (2016) 265 – 280.

[31] N. Shibata, T. Seki, G. Sanchez-Santolino, S. D. Findlay, Y. Kohno, T. Matsumoto, R. Ishikawa, Y. Ikuhara, Electric field imaging of single atoms, Nature communications 8 (2017) 15631.

[32] T. Seki, G. Sanchez-Santolino, R. Ishikawa, S. D. Findlay, Y. Ikuhara, N. Shibata, Quantitative electric field mapping in thin specimens using a segmented detector: Revisiting the transfer function for differential phase contrast, Ultramicroscopy 182 (2017) 258 – 263.

[33] M. Lohr, R. Schregle, M. Jetter, C. Wächter, K. Müller-Caspary, T. Mehrtens, A. Rosenauer, I. Pietzonka, M. Strassburg, J. Zweck, Quantitative measurements of internal electric fields with differential phase contrast microscopy on ingan/gan quantum well structures, physica status solidi (b) 253 (2016) 140–144.

[34] I. Lazic, E. G. Bosch, S. Lazar, M. Wirix, E. Yücelen, Integrated differential phase contrast (idpc)–direct phase imaging in stem for thin samples, Microscopy and Microanalysis 22 (2016) 36—-37.

[35] E. Yücelen, I. Lazic, E. G. T. Bosch, Phase contrast scanning transmission electron microscopy imaging of light and heavy atoms at the limit of contrast and resolution, Scientific Reports 8 (2018) 2676.

[36] T. Seki, G. Sanchez-Santolino, R. Ishikawa, S. D. Findlay, Y. Ikuhara, N. Shibata, Quantitative electric field mapping in thin specimens using a segmented detector: Revisiting the transfer function for differential phase contrast, Ultramicroscopy 182 (2017) 258–263.

[37] E. G. Bosch, I. Lazic, Analysis of hr-stem theory for thin specimen, Ultramicroscopy 156 (2015) 59 – 72.

[38] T. Seki, Y. Ikuhara, N. Shibata, Theoretical framework of statistical noise in scanning transmission electron microscopy, Ultramicroscopy 193 (2018) 118–125.

[39] K. Müller-Caspary, T. Mehrtens, M. Schowalter, T. Grieb, A. Rosenauer, F. F. Krause, C. Mahr, P. Potapov, ImageEval. A software for the processing, evaluation and acquisition of (S)TEM images, American Cancer Society, 2016, pp. 481–482. URL: https://onlinelibrary.wiley.com/doi/abs/10.1002/9783527808465.EMC2016.6143. doi:10.1002/9783527808465.EMC2016.6143. arXiv:https://onlinelibrary.wiley.com/doi/pdf/10.1002/9783527808465.EMC2016.6143.

[40] R. F. W. Bader, Atoms in Molecules: a Quantum Theory, New York: Oxford University Press, 1990.

[41] R. F. W. Bader, A quantum theory of molecular structure and its applications, Chemical Reviews 91 (1991) 893–928.

[42] R. Close, Z. Chen, N. Shibata, S. Findlay, Towards quantitative, atomic-resolution reconstruction of the electrostatic potential via differential phase contrast using electrons, Ultramicroscopy 159, Part 1 (2015) 124 – 137.

[43] I. Lazić, E. G. Bosch, S. Lazar, Phase contrast {STEM} for thin samples: Integrated differential phase contrast, Ultramicroscopy 160 (2016) 265 – 280.

[44] K. Müller-Caspary, M. Duchamp, M. Rösner, V. Migunov, F. Winkler, H. Yang, M. Huth, R. Ritz, M. Simson, S. Ihle, H. Soltau, T. Wehling, R. E. Dunin-Borkowski, S. Van Aert, A. Rosenauer, Atomic-scale quantification of charge densities in 2D materials, Physical Review B 98 (2018) 121408.

[45] A. Clausen, D. Weber, probonopd, J. Caron, M. Nord, K. Müller-Caspary, C. Ophus, R. Dunin-Borkowski, Libertem/libertem: 0.1.0, 2018. URL: https://doi.org/10.5281/zenodo.1478763. doi:10.5281/zenodo.1478763.

[46] F. Schwarzhuber, P. Melzl, S. Pöllath, J. Zweck, Introducing a non-pixelated and fast centre of mass detector for differential phase contrast microscopy, Ultramicroscopy 192 (2018) 21–28.